

Article

Capture Power Prediction of the Frustum of a Cone Shaped Floating Body Based on BP Neural Network

Wei Wang ¹ , Yanjun Liu ^{1,2,3,*}, Fagang Bai ¹ and Gang Xue ¹

¹ Institute of Marine Science and Technology, Shandong University, Qingdao 266200, China; wangwei_sdu@mail.sdu.edu.cn (W.W.); baifagang14@163.com (F.B.); xuegangzb@163.com (G.X.)

² School of Mechanical Engineering, Shandong University, Jinan 250061, China

³ Key Laboratory of High Efficiency and Clean Mechanical Manufacture, Ministry of Education, Jinan 250061, China

* Correspondence: lyj111ky@163.com

Abstract: How to improve the power generation of wave energy converters (WEC) has become one of the main research objectives in wave energy field. This paper illustrates a framework on the use of back propagation (BP) neural network in predicting capture power of the frustum of a cone shaped floating body. Mathematical model of single floating body is derived, and radius, semi-vertical angle, mass, submergence depth, power take-off (PTO) damping coefficient, and stiffness coefficient are identified as key variables. Commercial software ANSYS-AQWA is used for numerical simulations to obtain hydrodynamic parameters, and then capture power is calculated by these parameters. A database containing 100 samples is established by Latin hypercube sampling (LHS) method, and a simple feature study is conducted. A BP neural network model with high accuracy is designed and trained for predictions based on built database. The results show that forecasting results and desired outputs are in great agreement with error percentage not greater than 4%, correlation coefficient (CC) greater than 0.9, P value close to 1, and root mean square error (RMSE) less than 139 W. The proposed method provides a guideline for designers to identify basic parameters of the floating body and system damping coefficient.

Keywords: structure parameters; ANSYS-AQWA simulations; feature study; BP neural network; power predictions



Citation: Wang, W.; Liu, Y.; Bai, F.; Xue, G. Capture Power Prediction of the Frustum of a Cone Shaped Floating Body Based on BP Neural Network. *J. Mar. Sci. Eng.* **2021**, *9*, 656. <https://doi.org/10.3390/jmse9060656>

Academic Editor: Spyros A. Mavrakos

Received: 7 May 2021
Accepted: 10 June 2021
Published: 13 June 2021

Publisher's Note: MDPI stays neutral with regard to jurisdictional claims in published maps and institutional affiliations.



Copyright: © 2021 by the authors. Licensee MDPI, Basel, Switzerland. This article is an open access article distributed under the terms and conditions of the Creative Commons Attribution (CC BY) license (<https://creativecommons.org/licenses/by/4.0/>).

1. Introduction

Wave energy converters (WEC), a new type of energy extractor with little pollution, are expected to be a reliable alternative to the current generation method. There are two stages for an oscillating body WEC transforming wave energy into other forms of energy like electricity. A floating body is firstly required to capture the wave energy induced by a wave's motion. Then the moving floating body drives a generator to generate power. An intact oscillating body WEC system is generally composed of a moving floating body, a power take-off (PTO) system, and an anchor chain, etc. At present, the conversion efficiency of WECs is relatively low, so the main research objective is to improve the power generation of a specific device.

One method is to design a different floating body's shape, and the shape is usually irregular curved surface. McCabe [1] researched the optimization of the shape of a wave energy collector to improve energy extraction by genetic algorithms, and a benchmark collector shape was identified. Colby [2] used evolutionary algorithms to optimize the ballast geometry and achieved 84% improvement in power output. Fang [3] designed a mass-adjustable float, and a new optimization calculation method was proposed. Multi-freedom buoys have been also proposed in [4–6]. They can translate or rotate in more than one freedom, so more wave energy can be captured. Another means is to design an innovative PTO system. Reabroy [7] proposed a novel floating device integrated with a

fixed breakwater. The simulations and experiments proved that installing a breakwater can greatly improve the conversion efficiency. Liang [8] designed a novel PTO system which is inside the buoy with a mechanical motion rectifier (MMR). This mechanism can convert the bidirectional wave motion into unidirectional rotation of the generator by two one-way bearings. Li [9] improved this device by substituting one-way bearings for two one-way clutches. Chen [10] proposed a new point-absorber WEC with an outer-floater and a built-in power take-off mechanism. Besides, array-type WECs, integrated with many buoys and PTO systems, are also researched to achieve large scale power generation. The typical one is WaveNET [11], developed by Albatern in Scotland. Sun [12] proposed an array-type energy-capturing mechanism integrated with marine structures. Liu [13] proposed an array-type WEC combined with oscillating buoy.

The factors that affect the power generation have also been studied recently. Zou [14] analyzed the effects of spring force, mass force, and damping force on energy conversion efficiency based on a 3D wave tank model. Yu [15] and Wu [16] discussed the influence of the floating body's shape, PTO damping coefficient, system stiffness coefficient, and geometry parameters on power generation. Zheng [17] established an optimization model of energy conversion performance via genetic algorithm. Ma [18] researched the two-body floating point absorber and the results showed that stiffness coefficient had less effect on the power generation than damping coefficient. Ji [19] proved that PTO damping coefficient and submerged body volume were the most important parameters that affect the output power, and that the significant wave height had little influence on conversion efficiency. Tongphong [20] analyzed the effects of wave frequency, PTO damping coefficient, and structure form (floating or fixed) on capture factors.

Wave load and hydrodynamic parameters are vital factors in the analysis process of floating body's motions. Numerical simulations are widely used in hydrodynamic performance analysis to obtain these parameters. Ma [21] used ANSYS-AQWA software to assess the hydrodynamic performance and energy conversion of a pitching float WEC and analyzed key factors' influences on the performance. Amiri [22] presented a numerical simulation scheme for a point wave absorber and analyzed its performance. Yu [23] applied Reynolds-Averaged Navier-Stokes (RANS) computational method for analyzing the hydrodynamic heave response of a specific WEC device.

In addition to the traditional physical model [24,25], novel methods and models based on big data and machine learning have also been presented. Law [26] carried out wave prediction over a large distance downstream using artificial neural network, introducing machine learning algorithm into ocean engineering. Desouky [27] utilized non-linear autoregressive with exogenous input network to predict the surface elevation with the help of an ahead located sensor. Kumar [28] used the Minimal Resource Allocation Network (MRAN) and the Growing and Pruning Radial Basis Function (GAP-RBF) network to predict the daily wave heights based on real marine data. Some elevating measurements are also proposed to assess the performance of predictions in [29]. Avila [30] combined Fuzzy Inference Systems (FIS) and Artificial Neural Networks (ANN) to forecast wave energy in Canary Islands. Wang [31] predicted power outputs of a WEC in shallow water, taking bottom effects into accounts. Halliday [32] utilized Fast Fourier Transform (FFT) to predict wave behavior in short term based on real marine data. Davis [33] used a nonlinear Extended Kalman Filter to estimate the wave excitation force based on experimental wave tank data. Ni [34] combined the Long Short-Term Memory (LSTM) algorithm and the principal component analysis (PCA) together to predict the power generation of a WEC.

Different from traditional mathematical model, this paper presents an agent model using BP neural network to determine the complex non-linear reflection between design variables and power generation. Power predictions are the foundation of multi-objective optimizations of a floating body. Accurate power prediction can provide a guide for the electricity consumption, allocation, and distribution in power grid. Through the prediction, the unknown generation power becomes measurable, so reasonable manners can be arranged to increase the grid capacity.

The remainder of this paper is organized as follows: Section 2 develops the mathematical model of the oscillating float-type WEC. In Section 3, a sample database is established by LHS method, and a simple feature study is conducted. The geometric model and simulations of each sample are done in ANSYS-AQWA (developed by ANSYS company, based in Canonsburg, Pennsylvania, USA) in Section 4. Section 5 designs a BP neural network model and it is used to predict the capture power. Results and discussion are given in Section 6 and conclusions are presented in Section 7.

2. Mathematical Model

A schematic diagram of the oscillating body WEC is shown in Figure 1. To simplify the study, some assumptions are made as below:

1. linear wave theory and potential flow theory are suitable for this model, and they are used to describe wave motion;
2. only the heave motion of the floating body is considered;
3. the viscous force and mooring force acting on the floating body are ignored [10];
4. the PTO system is linear.

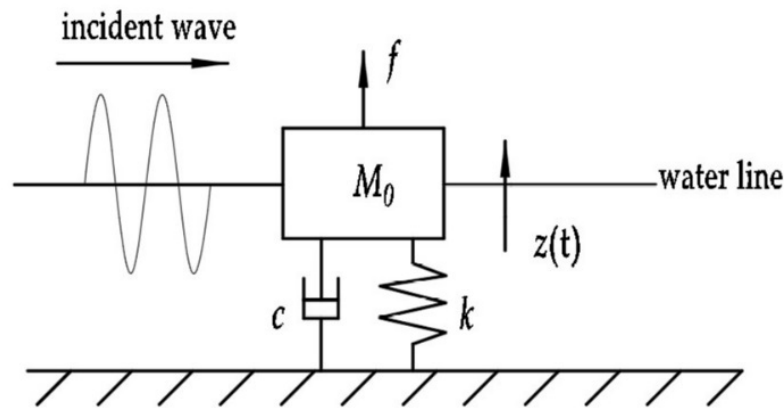


Figure 1. Mechanical model.

Under three assumptions, the following forces act on the floating body: hydrodynamic forces (excitation and radiation force); hydrostatic buoyancy; PTO damping force; rigid restoring force. According to the theory of fluid mechanics and Newton’s law, the governing equation of the floating body can be expressed as follows:

$$M_0\ddot{z}(t) = f_E - f_R - f_S - f_{PTO} - f_K \tag{1}$$

where M_0 represents mass; $z(t)$ represents the heave displacement; f_E represents excitation force; f_R represents radiation force; f_S represents hydrostatic buoyancy; f_{PTO} represents PTO damping force; f_K represents rigid restoring force.

The excitation force imparts on the floating body by the incoming wave. It is the summation of the Froude-Krylov force f_{FK} and the diffraction force f_D , so it can be written as follows:

$$f_E = f_{FK} + f_D \tag{2}$$

The radiation force is induced by the floating body’s motion and can be decomposed into an added mass term and a radiation damping term [25], so it can be expressed as follows:

$$f_R = A_M\ddot{z}(t) + B_C\dot{z}(t) \tag{3}$$

where A_M and B_C are the added mass and radiation damping in the vertical direction, respectively.

The hydrostatic buoyancy, induced by seawater static pressure, is the resultant force of gravity and buoyancy. It is a force that restores the structure to hydrostatic equilibrium and is linear with the heave displacement of the floating body. It can be written as:

$$f_S = \rho g A_W z(t) \tag{4}$$

where ρ is seawater density; g is acceleration of gravity; A_W is water cross area of the floating body. In this paper, the value of PTO damping is relatively large, and the heave displacement of the floating body is small. As a result, it is assumed that the water cross area of the floating body does not change. It is the section where the water line is located when the floating body is in still water. Therefore, the hydrostatic buoyancy can be expressed as:

$$f_S = \frac{1}{4} \pi \rho g D^2 z(t) \tag{5}$$

where D is the diameter of the floating body.

The energy conversion system can be simplified to a linear spring damping system, so the PTO damping force is

$$f_{PTO} = c \dot{z}(t) \tag{6}$$

where c is the damping coefficient of the PTO system.

The rigid restoring force is proportional to the heave displacement, and it can be written as follows:

$$f_k = k z(t) \tag{7}$$

where k is stiffness coefficient.

Reformulate Equation (1) through Equations (2), (3), (5)–(7):

$$[M_0 + A_M] \ddot{z}(t) + (B_C + c) \dot{z}(t) + (\rho g A_W + k) z(t) = f_E(t) \tag{8}$$

Apply Fourier transform to Equation (8) and obtain another governing equation in the frequency domain. It is

$$\left[(\rho g A_W + k) + j\omega(B_C + c) - \omega^2(M_0 + A_M) \right] Z(\omega) = F_E(\omega) \tag{9}$$

where ω is the wave frequency; j is imaginary unit; $Z(\omega)$ and $F_E(\omega)$ are functions of displacement and excitation force in the frequency domain, respectively.

In the frequency domain, the excitation force can be expressed by the product of the unit excitation force and the incident wave amplitude [35]. It is

$$F_E(\omega) = F_{unit}(\omega) A(\omega) \tag{10}$$

Equation (9) can be rewritten as follows:

$$\left[(\rho g A_W + k) + j\omega(B_C + c) - \omega^2(M_0 + A_M) \right] Z(\omega) = F_{unit}(\omega) A(\omega) \tag{11}$$

Formula (11) is a typical damped and forced vibration equation, so the natural frequency and damping factor can be expressed as below:

$$\omega_n = \sqrt{\frac{\rho g A_W + k}{M_0 + A_M}} \tag{12}$$

$$\beta_n = \frac{B_C + c}{2(M_0 + A_M)} \tag{13}$$

From Equations (12) and (13), the natural frequency and damping factor of a given WEC change over added mass and added damping.

According to Equation (11), the heave response in the frequency domain is

$$Z(\omega) = \frac{F_{unit}(\omega)A(\omega)}{(\rho g A_W + k) + j\omega(B_C + c) - \omega^2(M_0 + A_M)} \tag{14}$$

The average power in one wave period, captured by the floating body with heave motion, can be written as the product of damping force and vertical velocity. The work done by damping force is the energy absorbed by the floating body, so the mean capture power is

$$\begin{aligned} P_{mean} &= \frac{1}{T} \int_0^T f_{PTO} \dot{z}(t) dt \\ &= \frac{1}{T} \int_0^T c \dot{z}(t)^2 dt \\ &= \frac{1}{2} \omega^2 c |Z(\omega)|^2 \\ &= \frac{1}{2} c \frac{\omega^2 |F_E|^2}{[-\omega^2(M_0 + A_M) + k + \rho g A_W]^2 + \omega^2(B_C + c)^2} \\ &= \frac{1}{2} c \frac{|F_E|^2}{[\frac{-\omega^2(M_0 + A_M) + k + \rho g A_W}{\omega}]^2 + (B_C + c)^2} \end{aligned} \tag{15}$$

The mean capture power reaches the maximum when the following conditions are met.

$$k = \omega^2(M_0 + A_M) - \rho g A_W \tag{16}$$

$$c = \begin{cases} B_C, & B_C > 0 \\ -B_C, & B_C < 0 \end{cases} \tag{17}$$

This stiffness and damping are called the best stiffness and the best damping, respectively. When $B_c > 0$, the natural frequency, damping factor, and displacement are

$$\omega_n = \omega \tag{18}$$

$$\beta_n = \frac{B_C}{M_0 + A_M} \tag{19}$$

$$Z(\omega) = -\frac{jF_{unit}(\omega)A(\omega)}{2\omega B_C} \tag{20}$$

The max capture power is

$$P_{max} = \frac{|F_E|^2}{8B_C} \tag{21}$$

3. Design of Experiments (DOE) Method

3.1. Latin Hypercube Sampling

The sampling method is of great importance in experimental design. A good sampling method can result in more reasonable sample distribution, leading to a better model with higher accuracy. In this paper, a Latin hypercube sampling (LHS) method is utilized to generate sample points. Different from random sampling, LHS has a high efficiency of space filling by maximizing the stratification of each edge distribution, which improves the uniformity.

According to Equation (15), the factors that determine the capture power under given wave conditions are PTO damping coefficient c , system stiffness coefficient k , wave exciting force F_E , float mass m , added mass A_M , and added damping B_C . Added mass, added damping, and wave exciting force are related to the geometry and submergence depth of the floating body. The geometric features of the floating body depend on radius R , semi-vertical angle α , and mass m . As a result, four main geometric parameters, including radius R , semi-vertical angle α , mass m , and submergence depth d , plus two system parameters, PTO damping coefficient c and stiffness coefficient k , are selected as key variables that affect the capture power.

The sample space of six key variables are defined as follows:

$$\left\{ \begin{array}{l} d \in [2, 3] \\ R \in [1.5, 3] \\ m \in [7000, 8000] \\ \alpha \in [5, 25] \\ c \in [10, 000, 30, 000] \\ k \in [3000, 6000] \end{array} \right. \quad (22)$$

A database covering 100 sample points is established (see in Appendix A) and scatter diagrams of these samples are shown in Figure 2.

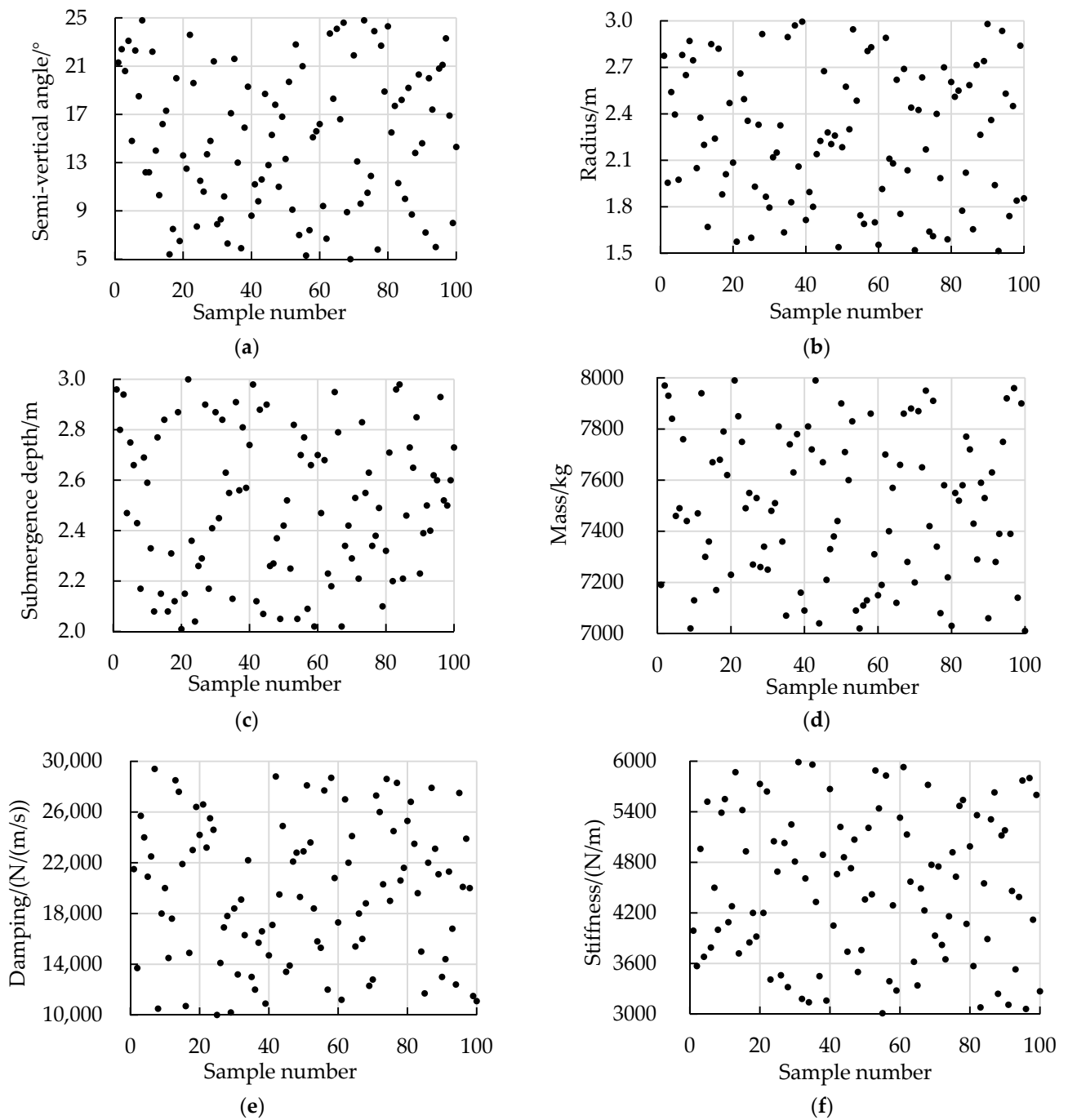


Figure 2. Sample scatter diagrams. (a) semi-vertical angle; (b) radius; (c) submergence depth; (d) mass; (e) damping; (f) stiffness.

In Figure 2, each variable fills the whole sample space and the standard deviation of the value is small. It can reflect the relationship between the factor and the response in the six spaces.

3.2. Feature Study

Suitable feature study on the data set can give an insight to the correlation between the inputs and output. Pearson correlation analysis is conducted in this section to identify the correlation between six key variables and the capture power. Figure 3 shows the correlation coefficients in different wave situations. In this heatmap, a negative value means a negative correlation, and a positive value means a positive correlation. A large absolute value means a strong correlation.

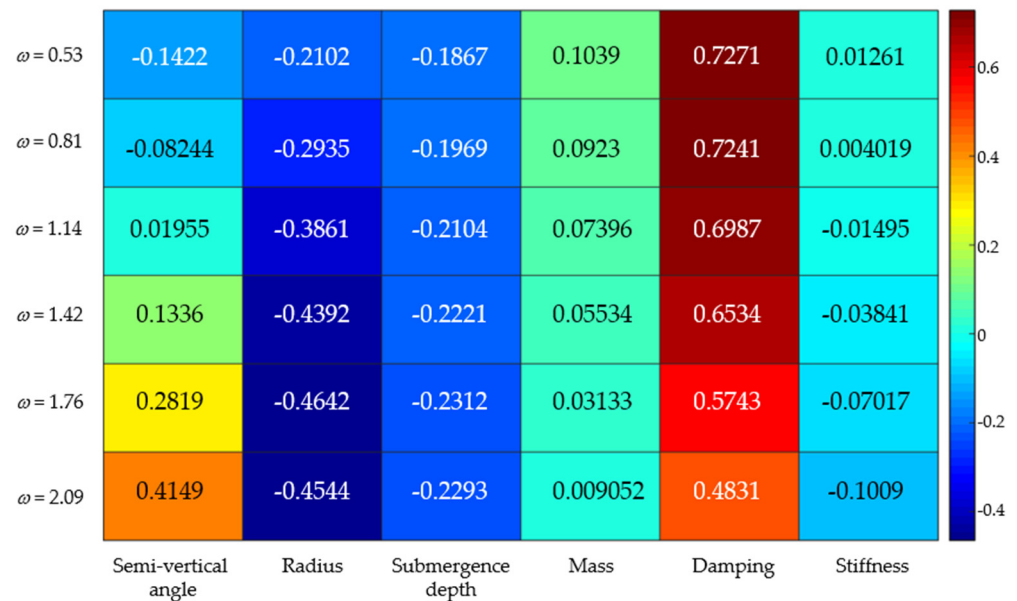


Figure 3. The correlation coefficients between the inputs and output.

In general, radius, submergence depth, and damping show a strong correlation, while semi-vertical angle, mass, and stiffness behave a weak correlation. Besides, the correlation is different at different wave frequency. When the wave frequency is 0.53 and 0.81 rad/s, semi-vertical angle shows a negative correlation, while a positive correlation comes up at other frequencies. The similar situation happens on stiffness. Mass and damping behave a positive correlation, while radius and submergence depth show a negative correlation all the time.

4. Numerical Simulations

4.1. Simulation Scheme

The structural schematic of the cone shaped floating body investigated in this study is shown in Figure 4.

The height of the cylinder part above the waterline is a constant, 0.5 m. In ANSYS Design Modeler, the 3D geometry with given parameters is created.

In this paper, ANSYS-AQWA, a commercial computation software based on potential flow theory, is utilized to calculate hydrodynamic parameters. The simulation process, including numerical modeling, parameters setting, mesh generation, and data post-processing, can be conducted in the graphical interface directly. The basic simulation steps for each sample are as follows:

1. The moment of inertia and center of mass of the floating body are calculated in Static Structural module;

2. Set solution environment in hydrodynamic diffusion module. The water line is at $z = 0$, the seawater depth is 200 m, and the surface area are $100 \text{ m} \times 100 \text{ m}$. Details of the point mass, additional damping, and additional hydrostatic stiffness are set according to the results obtained in Static Structural module and parameters in Table A1. In this study, the considered wave range is from 0 to 0.4 Hz, meaning that the wave circular frequency within 2.5 rad/s needs to be simulated. Therefore, the defeaturing tolerance and maximum element size are 0.5 m and 1 m, respectively. The maximum allowed wave frequency is 0.61 Hz in this scheme;
3. Solve the model in the frequency domain and obtain Diffraction and Froude-Krylov force F_e , added mass A_M , and radiation damping B_C .

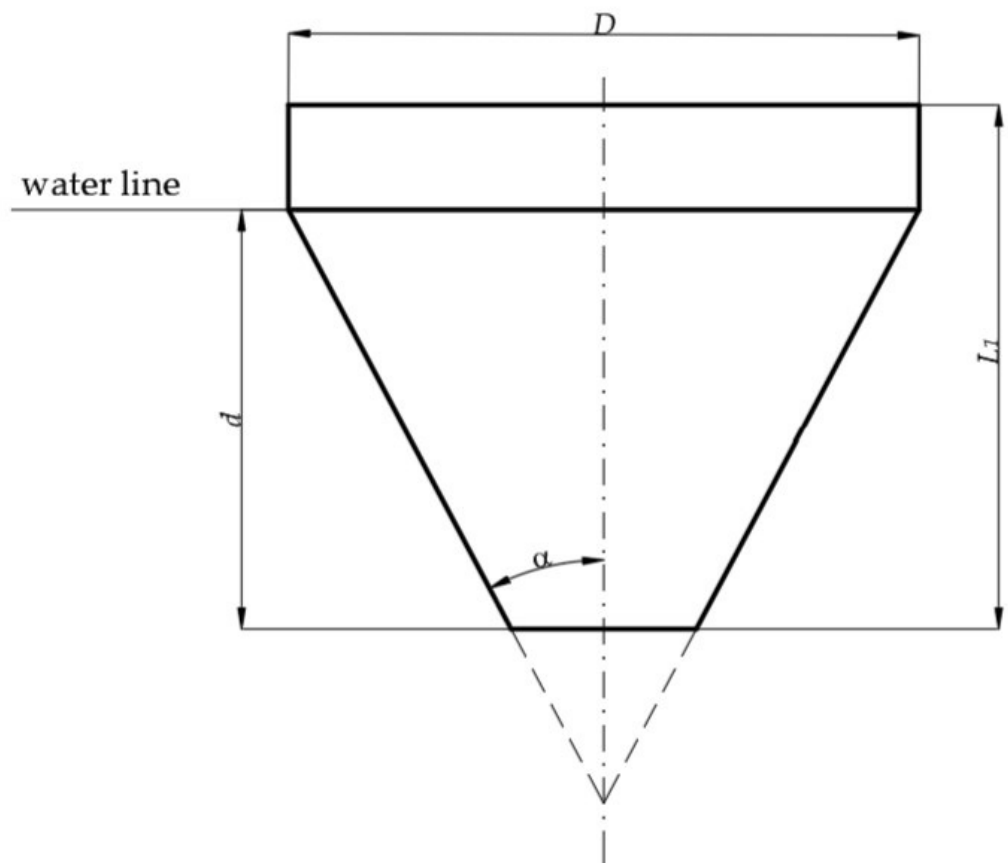


Figure 4. Schematic of the floating body's structure.

For each simulation, the given frequency range is divided into 52 frequency points. The mean power for each sample at each frequency is calculated. The results of sample 1 and sample 2 are shown in Figure 5.

With the increase in wave frequency, the capture power rises firstly and then drops steadily. For each sample, there is a unique optimal frequency in which the capture power can reach the maximum. The 100 samples' capture power are calculated so that they can be used as training set and test set for BP neural network. Only two samples' results are presented in this figure.

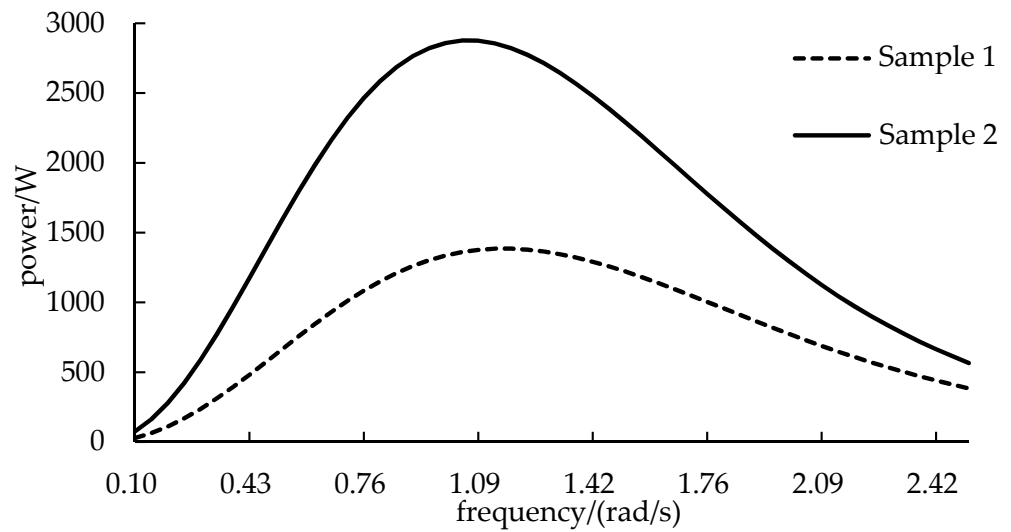


Figure 5. Mean capture power of sample 1 and sample 2.

4.2. Theoretical Verification of Simulations

Falnes [36] illustrated that the maximum power that a heaving axisymmetric body can absorb is

$$P_{max} = \frac{J\lambda}{2\pi} \tag{23}$$

where J is the wave energy flux; λ is the wavelength. For deep-water waves, $\lambda = g/2\pi$. J is

$$J = \frac{\rho g^2 T H^2}{32\pi} \tag{24}$$

where T and H are wave period and height, respectively. Budal’s upper bound [36] gave another upper limit power that a submerged body with given volume V can absorb. It is

$$P_u < \frac{\pi\rho g V H}{4T} \tag{25}$$

where V is the volume of the submerged part. The point of intersection of two theoretical curves can be defined as (T_c, P_c) . P_c is

$$P_c = \frac{\rho g^2}{32\pi} \sqrt{2VH^3} \tag{26}$$

In this study, Equations (23) and (25) are used to verify the validity of simulations. To make comparisons, the results are normalized by dividing P_c . The three curves are shown in Figure 6.

It can be found that the capture power curves of two samples are in the area enclosed by curve P_{max} , curve P_u , and coordinate axes, which means the simulation scheme is accurate and reliable. All the samples are verified successfully and only two of them are demonstrated in this section.

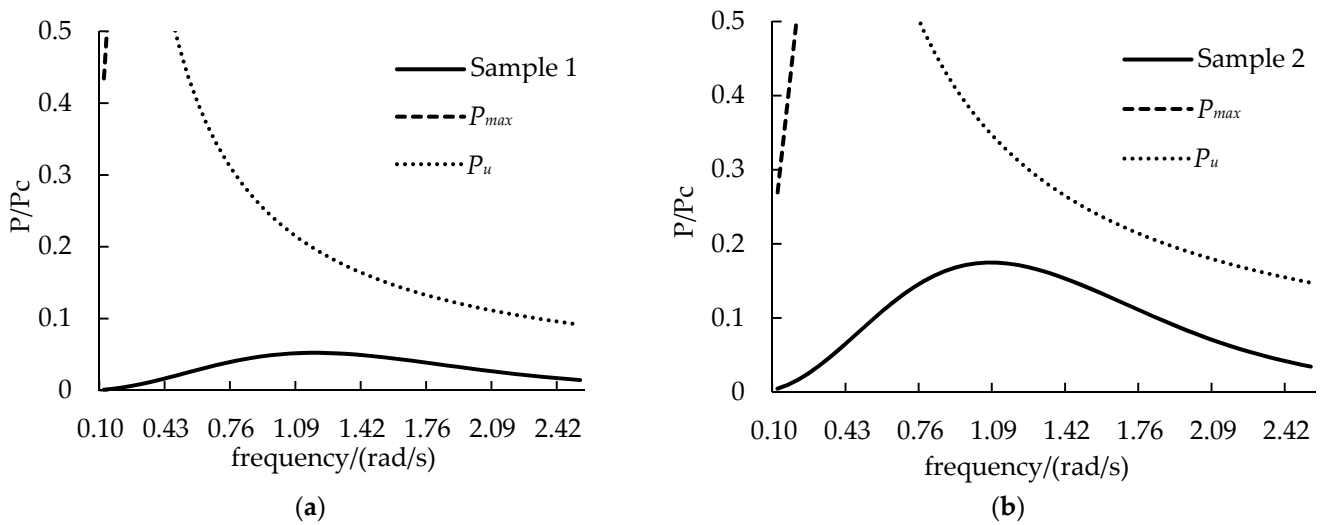


Figure 6. Power curves from simulations and theories. (a) results of sample 1; (b) results of sample 2.

5. BP Neural Network

The back propagation (BP) neural network is a kind of feedforward neural network trained by error back propagation algorithm. It is a most widely used form, and is composed of many nonlinear transformation units. This algorithm has a strong non-linear mapping ability and can simulate any nonlinear continuous functions with much higher accuracy theoretically. After the network is trained, the reflection between the inputs and outputs can be obtained and memorized. They are shown on the weights of each layer. BP neural network’s structure is flexible, which means the number of layers and neurons can be changed according to research objectives. A BP neural network generally includes an input layer, one or two hidden layers, and an output layer. Full connections are applied between layers. More details about BP neural network can be seen in [37].

5.1. Neural Network Design

The first step to design a good neural network is to identify the number of hidden layers. A three layers neural network, which contains only one hidden layer, can simulate any reflection from n -dimensional inputs to m -dimensional outputs. Hence, a three-layer neural network with one hidden layer is selected in this study. Next, the nodes of each layer need to be identified. In this study, six key variables are selected, so the number of nodes in input layer is six. Only one parameter, capture power, needs to be predicted, so the number of nodes in output layer is one. Finally, the number of nodes in hidden layer needs to be identified. There is an empirical formula [38] that can be referred to identify the number of hidden nodes.

$$l = \sqrt{n + m} + a \tag{27}$$

where l , n , and m are the number of nodes in hidden layer, input layer, and output layer, respectively; a is an adjustment constant ranging from 1 to 10.

In this paper, the number of hidden nodes is tested from 3 to 12 to identify the most suitable value. MSE is used to evaluate the performance, and the results are shown in Table 1.

Table 1. The number of hidden nodes and the values of MSE.

Number of Nodes	3	4	5	6	7	8	9	10	11	12
MSE	0.0215	0.0160	0.0236	0.0238	0.0274	0.0263	0.0371	0.0338	0.0364	0.0341

MSE reaches a minimum when the number of hidden nodes is 4, which is the optimal value for this case. The final BP neural network structure designed in this paper is shown in Figure 7.

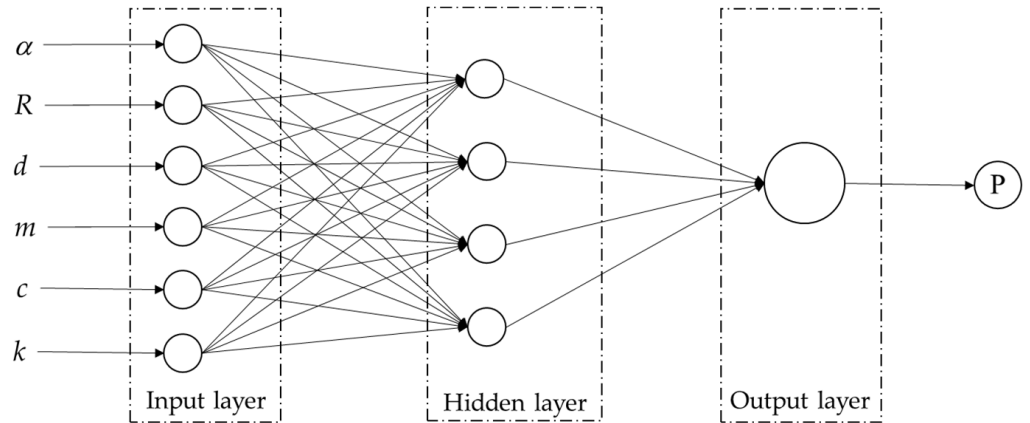


Figure 7. Structure of the designed BP neural network.

According to the structure, the output b_j of input layer can be expressed as follows:

$$b_j = f_1\left(\sum_{i=1}^6 w_{ij}x_i + \theta_j\right), j = 1, 2, 3, 4 \tag{28}$$

where w_{ij} is the weight from the input layer to the hidden layer; x_i is the input variable; θ_j is the threshold value of the hidden layer. The output y of the BP neural network is

$$y = f_2\left(\sum_{j=1}^4 w_j b_j + \theta'\right), j = 1, 2, 3, 4 \tag{29}$$

where w_j is the weight from the hidden layer to the output layer; θ' is the threshold value of the output layer.

5.2. Data Standardization and Neural Network Training

Before training, data standardization for individual features needs to be conducted to improve training speed. The standardization formula used in this paper is

$$x = \frac{x_i - x_{\min}}{x_{\max} - x_{\min}} \tag{30}$$

where x is the standardized result; x_{\max} and x_{\min} are the maximum and minimum values in the dataset, respectively. The standardized data have a distribution range between 0 and 1.

The network training process is to adjust the weights and thresholds so that the value of loss function reduces to a minimum. The training parameters for this model are shown in Table 2.

Table 2. Training parameters.

Weight Change Rate	Learning Rate	Training Epochs	Performance (Judged by Mean Square Error)	Minimum Gradient	Validation Checks
0.01	0.05	1000	10^{-5}	10^{-7}	6

Tangent sigmoid function (*tansig*) is adopted for the hidden layer, and the linear function (*purelin*) is adopted for the output layer. In the training process, mean squared error is used as loss function. It is defined as

$$MSE = \frac{1}{m} \sum_{i=1}^m (\hat{y} - y)^2 \tag{31}$$

where m is the number of samples; \hat{y} is the observed value; y is the real value. In this paper, the top 80 samples are defined as training set. This model is trained in MATLAB R2019a, and the trendline of MSE for training set is shown as Figure 8.

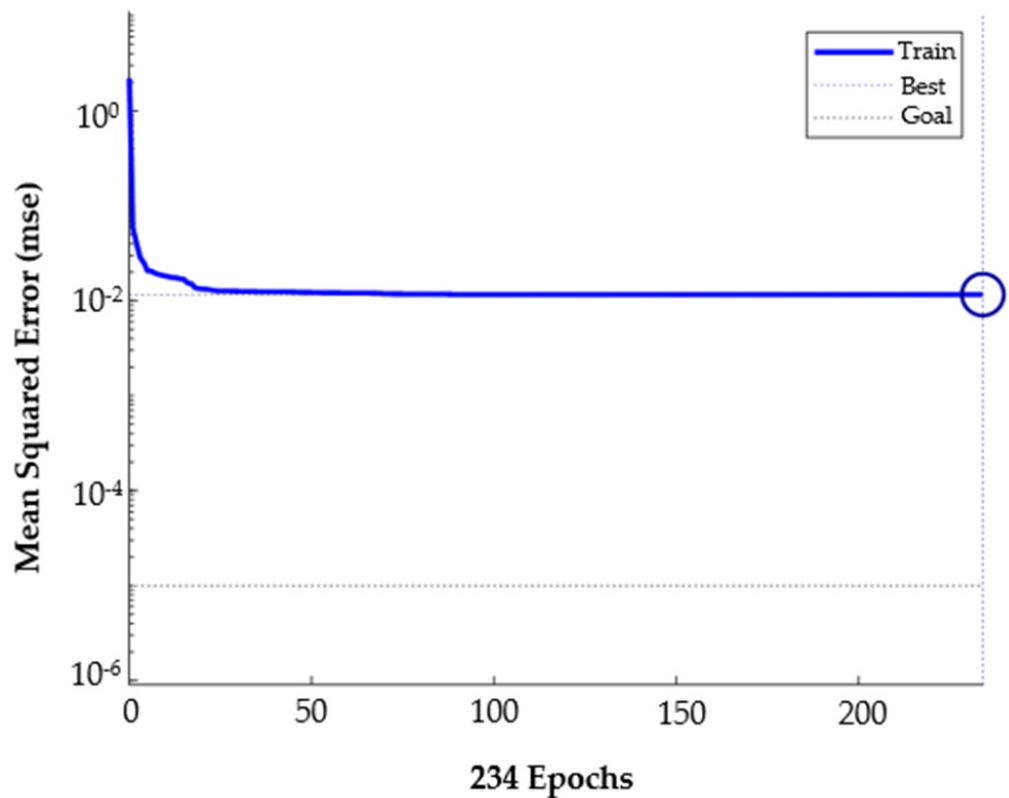


Figure 8. The trendline of training loss versus epochs.

The training process is terminated at 234 epochs because the gradient reaches the minimum (10^{-7}). The rest 20 samples are used to test, and the forecasting results after being de-standardized are shown in the next section.

6. Results and Discussion

In this section, six groups’ forecasting data ($\omega = 0.53$ rad/s, $\omega = 0.81$ rad/s, $\omega = 1.14$ rad/s, $\omega = 1.42$ rad/s, $\omega = 1.76$ rad/s, and $\omega = 2.09$ rad/s) is given because they are the most common wave frequency. The desired outputs and forecasting results are presented in Figure 9 under different frequency. For each sample, the output power at 52 frequency points can be predicted.

In Figure 9a, the deviation of five samples (85, 90, 94, 99, and 100), which are at the lowest position of the graph, are relatively large, with mean error about 60 W. In Figure 9c, the error of sample 81 is the largest, with approximately 500 W. The forecasting results of sample 95 and 96 are rather larger than desired outputs in Figure 9d,f, and the error of sample 89 is around 200 W in Figure 9f. The highest accuracy is at $\omega = 0.81$ rad/s and almost all the forecasting points fit the desired points. In contrast, the worst result is at $\omega = 2.09$ rad/s and there are five forecasting results deviating the desired outputs.

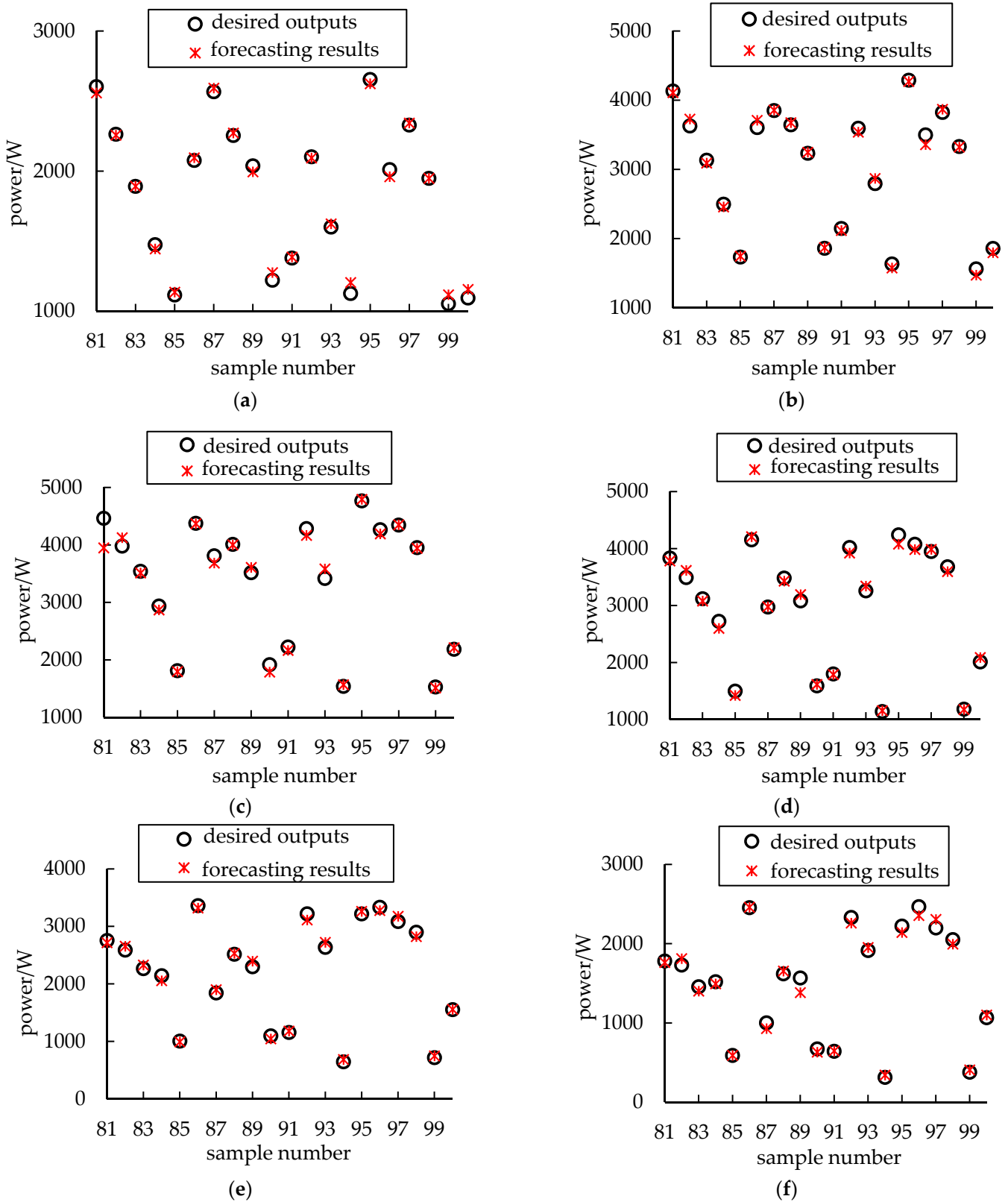


Figure 9. Comparisons between desired outputs and forecasting results. (a) $\omega = 0.53$ rad/s; (b) $\omega = 0.81$ rad/s; (c) $\omega = 1.14$ rad/s; (d) $\omega = 1.42$ rad/s; (e) $\omega = 1.76$ rad/s; (f) $\omega = 2.09$ rad/s.

To further verify the accuracy of the BP model, correlation coefficient (CC), root mean square error (RMSE), and error percentage are introduced in this section. They are defined as follows [29]

$$CC = \frac{\sum_{i=1}^m (t_i - \bar{t})(y_i - \bar{y})}{\sqrt{\sum_{i=1}^m (t_i - \bar{t})^2 \sum_{i=1}^m (y_i - \bar{y})^2}} \tag{32}$$

$$RMSE = \sqrt{\frac{1}{m} \sum_{i=1}^m (t_i - y_i)^2} \tag{33}$$

$$e = \frac{1}{m} \sum_{i=1}^m \left| \frac{y_i - t_i}{t_i} \right| \tag{34}$$

where m is the number of forecasting results; t_i is the desired value; y_i is the output of the network; \bar{t} and \bar{y} are average values of desired and forecasting results, respectively. The significance analysis of ANOVA is also conducted in MATLAB R2019a, and the statistical parameters (after de-standardization) are listed in Table 3.

Table 3. The statistical parameters between desired and forecasting results.

Wave Frequency (rad/s)	CC	RMSE (W)	Error Percentage	p Value
0.53	0.95931	37.5	2.03%	0.9588
0.81	0.90129	60.5	1.79%	0.9769
1.14	0.92105	138.7	2.45%	0.9206
1.42	0.91295	78.8	2.22%	0.9691
1.76	0.92558	61.6	2.7%	0.9789
2.09	0.94852	69.3	4%	0.9362

The values of CC are greater than 0.9, meaning that the correlations with each group are well fitted. The values of RMSE do not exceed 140 W, and the error percentage is no more than 4%, indicating that desired outputs and forecasting results are reasonably fitted. All P values are close to 1, which means there is no significant difference between desired and forecasting outputs. These validation factors indicate that this model has a good prediction accuracy and meets the engineering requirement.

7. Conclusions

In this paper, capture power predictions of a specific shape floating body are attempted based on mathematical model, ANSYS-AQWA simulations, and BP neural network. The key variables are identified and the simulation scheme is proposed. A sample database is built by LHS and the corresponding power of each sample is calculated. In the end, a BP neural network, of which training set is from simulation results, is designed to predict the capture power at different wave frequency. Its performance and accuracy are also evaluated through statistical parameters.

According to the results, the conclusions can be given as follows:

1. A mathematical model is constructed to identify the most important factors that affect the capture power. Four geometric parameters (radius, semi-vertical angle, mass, and submergence depth) and two system parameters (PTO damping coefficient and stiffness coefficient) are identified as key variables;
2. A BP neural network with high accuracy is designed and it is used to predict the capture power. The error percentage of top five groups is less than 2.5%, and that of the last group is 4%. The values of CC are greater than 0.9 and that of RMSE are less than 80 W except for the third group, of which the value of RMSE is 138.7 W. The P values are close to 1. However, due to the error of simulations caused by commercial software, this method needs experimental data to support.

Author Contributions: Methodology, W.W.; Software, F.B.; Validation, W.W. and F.B.; Formal analysis, W.W.; Investigation, Y.L.; Resources, Y.L. and G.X.; Writing—original draft preparation, W.W.; Writing—review and editing, G.X.; Funding acquisition, Y.L. All authors have read and agreed to the published version of the manuscript.

Funding: This research was funded by the Joint Research Fund under cooperative agreement between the National Natural Science Foundation of China and Shandong Provincial People’s Government (grant number U1706230), Shandong Province Major Science and Technology Innovation Project (grant number 2018CXGC0104), Marine Renewable Energy Fund Project (grant number GHME2017YY01), and National Key Research and Development Plan (2017YFE0115000).

Institutional Review Board Statement: Not applicable.

Informed Consent Statement: Not applicable.

Data Availability Statement: Not applicable.

Acknowledgments: The authors gratefully acknowledge the financial support from the Joint Research Fund under cooperative agreement between the National Natural Science Foundation of China and Shandong Provincial People’s Government (grant number U1706230), Shandong Province Major Science and Technology Innovation Project (grant number 2018CXGC0104), Marine Renewable Energy Fund Project (grant number GHME2017YY01), and National Key Research and Development Plan (2017YFE0115000).

Conflicts of Interest: The authors declare no conflict of interest.

Appendix A

Table A1. Details of 100 sample points.

No.	α	R	d	m	c	k
1	21.3	2.775	2.96	7190	21,500	3990
2	22.4	1.955	2.80	7970	13,700	3570
3	20.6	2.540	2.94	7930	25,700	4960
4	23.1	2.395	2.47	7840	24,000	3680
5	14.8	1.975	2.75	7460	20,900	5520
6	22.3	2.780	2.66	7490	22,500	3790
7	18.5	2.650	2.43	7760	29,400	4500
8	24.8	2.870	2.17	7440	10,500	4000
9	12.2	2.745	2.69	7020	18,000	5390
10	12.2	2.050	2.59	7130	20,000	5550
11	22.2	2.375	2.33	7470	14,500	4090
12	14.0	2.200	2.08	7940	17,600	4280
13	10.3	1.670	2.77	7300	28,500	5870
14	16.2	2.850	2.15	7360	27,600	3720
15	17.3	2.240	2.84	7670	21,900	5420
16	5.4	2.820	2.08	7170	10,700	4930
17	7.5	1.880	2.31	7680	14,900	3850
18	20.0	2.010	2.12	7790	23,000	4200
19	6.5	2.470	2.87	7620	26,400	3920
20	13.6	2.085	2.01	7230	24,200	5730
21	12.5	1.575	2.15	7990	26,600	4200
22	23.6	2.660	3.00	7850	23,200	5640
23	19.6	2.495	2.36	7750	25,500	3410
24	7.7	2.355	2.04	7490	24,600	5050
25	11.5	1.600	2.26	7550	10,000	4690
26	10.6	1.930	2.29	7270	14,100	3460
27	13.7	2.330	2.90	7530	16,900	5030
28	14.8	2.915	2.17	7260	17,800	3320

Table A1. Cont.

No.	α	R	d	m	c	k
29	21.4	1.865	2.41	7340	10,200	5250
30	7.9	1.795	2.87	7250	18,400	4810
31	8.3	2.120	2.45	7480	13,200	5990
32	10.2	2.150	2.84	7510	19,100	3180
33	6.3	2.325	2.63	7810	16,300	4610
34	17.1	1.635	2.55	7360	22,200	3140
35	21.6	2.895	2.13	7070	13,000	5960
36	13.0	1.830	2.91	7740	12,000	4330
37	5.9	2.970	2.56	7630	15,700	3450
38	15.9	2.060	2.81	7780	16,600	4890
39	19.3	2.995	2.57	7160	10,900	3160
40	8.6	1.715	2.74	7090	14,700	5670
41	11.2	1.895	2.98	7810	17,100	4050
42	9.8	1.800	2.12	7720	28,800	4660
43	11.6	2.140	2.88	7990	19,500	5220
44	18.7	2.225	2.07	7040	24,900	4860
45	12.8	2.675	2.90	7670	13,400	3740
46	15.3	2.280	2.26	7210	13,900	4730
47	17.8	2.205	2.27	7330	22,100	5070
48	11.0	2.260	2.37	7380	22,800	3500
49	16.8	1.540	2.05	7440	19,300	3760
50	13.3	2.185	2.42	7900	22,900	4360
51	19.7	2.575	2.52	7710	28,100	5210
52	9.1	2.300	2.25	7600	23,600	4420
53	22.8	2.945	2.82	7830	18,400	5890
54	7.0	2.485	2.05	7090	15,800	5440
55	21.0	1.745	2.70	7020	15,300	3010
56	5.3	1.690	2.77	7110	27,700	5830
57	7.4	2.805	2.09	7130	12,000	3390
58	15.1	2.830	2.66	7860	28,700	4290
59	15.6	1.700	2.02	7310	20,800	3280
60	16.2	1.555	2.70	7150	17,300	5330
61	9.4	1.915	2.47	7190	11,200	5930
62	6.7	2.890	2.68	7700	27,000	5130
63	23.7	2.110	2.23	7400	22,000	4570
64	18.3	2.080	2.18	7570	24,100	3620
65	24.1	2.620	2.95	7120	15,400	3340
66	16.6	1.755	2.79	7660	18,000	4490
67	24.6	2.690	2.02	7860	16,000	4230
68	8.9	2.035	2.34	7280	18,800	5720
69	5.0	2.440	2.42	7880	12,300	4770
70	21.9	1.520	2.29	7200	12,800	3930
71	13.1	2.425	2.53	7870	27,300	4750
72	9.6	2.635	2.21	7650	26,000	3820
73	24.8	2.170	2.83	7950	20,300	3650
74	10.5	1.640	2.55	7420	28,600	4160
75	11.9	1.610	2.63	7910	19,000	4920
76	23.9	2.400	2.34	7340	24,500	4630
77	5.8	1.985	2.38	7080	28,300	5470
78	22.7	2.700	2.49	7580	20,600	5540
79	18.9	1.590	2.10	7220	21,600	4070
80	24.3	2.605	2.32	7030	25,300	4990
81	15.5	2.510	2.71	7550	26,800	3570
82	17.7	2.550	2.20	7520	23,500	5360
83	11.3	1.775	2.96	7580	19,600	3080
84	18.2	2.020	2.98	7770	15,000	4550
85	10.0	2.585	2.21	7720	11,700	3890

Table A1. Cont.

No.	α	R	d	m	c	k
86	19.2	1.655	2.46	7430	22,000	5310
87	8.7	2.715	2.73	7290	27,900	5630
88	13.8	2.265	2.65	7590	23,100	3240
89	20.3	2.740	2.85	7530	21,100	5120
90	14.6	2.980	2.23	7060	13,000	5180
91	7.2	2.360	2.39	7630	14,400	3110
92	20.0	1.940	2.50	7280	21,300	4460
93	17.4	1.515	2.40	7390	16,800	3530
94	6.0	2.935	2.62	7750	12,400	4390
95	20.8	2.530	2.60	7920	27,500	5770
96	21.1	1.740	2.93	7390	20,100	3060
97	23.3	2.450	2.52	7960	23,900	5800
98	16.9	1.840	2.50	7140	20,000	4120
99	8.0	2.840	2.60	7900	11,500	5600
100	14.3	1.855	2.73	7010	11,100	3270

References

- Mccabe, A.P.; Aggidis, G.A.; Widden, M.B. Optimizing the shape of a surge-and-pitch wave energy collector using a genetic algorithm. *Renew. Energy* **2010**, *35*, 2767–2775. [CrossRef]
- Colby, M.K.; Nasroullahi, E.M.; Tumer, K. Optimizing ballast design of wave energy converters using evolutionary algorithms. In Proceedings of the 13th Annual Genetic and Evolutionary Computation Conference (GECCO 2011), Dublin, Ireland, 12–16 July 2011; pp. 1739–1746.
- Fang, H.; Jin, L. Investigation on Resonance Response of Mass-Adjustable Float in Wave Energy Conversion System. *Energy Procedia* **2019**, *158*, 315–320. [CrossRef]
- Giorgi, G.; Ringwood, J.V. Analytical representation of nonlinear Froude-Krylov forces for 3-DoF point absorbing wave energy devices. *Ocean Eng.* **2018**, *164*, 749–759. [CrossRef]
- Le-Ngoc, L.; Gardiner, A.I.; Stuart, R.J.; Caughley, A.J.; Huckerby, J.A. Progress in the development of a multimode self-reacting wave energy converter. *OCEANS* **2010**, *2010*, 1–7.
- Gao, H.; Yu, Y. The dynamics and power absorption of cone-cylinder wave energy converters with three degree of freedom in irregular waves. *Energy* **2018**, *143*, 833–845. [CrossRef]
- Reabroy, R.; Zheng, X.; Zhang, L.; Zang, J.; Yuan, Z.; Liu, M.; Sun, K.; Tiaple, Y. Hydrodynamic response and power efficiency analysis of heaving wave energy converter integrated with breakwater. *Energy Convers. Manag.* **2019**, *195*, 1174–1186. [CrossRef]
- Liang, C.; Ai, J.; Zuo, L. Design, fabrication, Simulation and testing of an ocean wave energy converter with mechanical motion rectifier. *Ocean Eng.* **2017**, *136*, 190–200. [CrossRef]
- Li, X.; Martin, D.; Liang, C.; Chen, C.; Parker, R.G.; Zuo, L. Characterization and verification of a two-body wave energy converter with a novel power take-off. *Renew. Energy* **2020**, *163*, 910–920. [CrossRef]
- Chen, Z.; Zhou, B.; Zhang, L.; Li, C.; Zang, J.; Zheng, X.; Xu, J.; Zhang, W. Experimental and numerical study on a novel dual-resonance wave energy converter with a built-in power take-off system. *Energy* **2018**, *165*, 1008–1020. [CrossRef]
- WaveNET—the Floating, Flexible Wave Energy Generator. Available online: <https://newatlas.com/albatern-wavenet-squid-floating-wave-energy/34942/> (accessed on 22 April 2021).
- Sun, P.; Li, Q.; He, H.; Chen, H.; Zhang, J.; Li, H.; Liu, D. Design and optimization investigation on hydraulic transmission and energy storage system for a floating-array-buoys wave energy converter. *Energy Convers. Manag.* **2021**, *235*, 113998. [CrossRef]
- Liu, Z.; Qu, N.; Han, Z.; Zhang, J.; Zhang, S.; Li, M.; Shi, H. Study on energy conversion and storage system for a prototype buoys-array wave energy converter. *Energy Sustain. Dev.* **2016**, *34*, 100–110. [CrossRef]
- Zou, J. Numerical Simulation of Wave Energy Use Efficiency of Oscillating Buoy and Its Influence Parameters. Master’s Dissertation, Harbin Institute of Technology, Harbin, China, December 2014.
- Yu, L. The Performance Research on the Oscillating Float Type Wave Energy Converter. Master’s Dissertation, Harbin Engineering University, Harbin, China, March 2016.
- Wu, L. Study on Hydrodynamic Performance and Energy Conversion Efficiency of a Three-Dimensional Two-Body WEC. Master’s Dissertation, Harbin Engineering University, Harbin, China, March 2017.
- Zheng, X. Study on the Hydrodynamic Performance for Two Kinds of Point Absorbing Wave Energy Device. Doctor’s Dissertation, Harbin Engineering University, Harbin, China, June 2016.
- Ma, Y.; Zhang, A.; Yang, L.; Li, H.; Zhai, Z.; Zhou, H. Motion simulation and performance analysis of two-body floating point absorber wave energy converter. *Renew. Energy* **2020**, *157*, 353–367. [CrossRef]
- Ji, X.; Shami, E.A.; Monty, J.; Wang, X. Modelling of linear and non-linear two-body wave energy converters under regular and irregular wave conditions. *Renew. Energy* **2020**, *147*, 487–501. [CrossRef]

20. Tongphong, W.; Kim, B.H.; Kim, I.C.; Lee, Y.H. A study on the design and performance of ModuleRaft wave energy converter. *Renew. Energy* **2021**, *163*, 649–673. [[CrossRef](#)]
21. Ma, Y.; Ai, S.; Yang, L.; Zhang, A.; Liu, S.; Zhou, B. Research on design and optimization of the pitching float wave energy converter. *Energy Sci. Eng.* **2020**, *8*, 3866–3882. [[CrossRef](#)]
22. Amiri, A.; Panahi, R.; Radfar, S. Parametric study of two-body floating-point wave absorber. *J. Mar. Sci. Appl.* **2016**, *15*, 41–49. [[CrossRef](#)]
23. Yu, Y.; Li, Y. A RANS Simulation of the Heave Response of a Two-Body Floating-Point Wave Absorber. In Proceedings of the 21st International Offshore and Polar Engineering Conference, Maui, HI, USA, 19–24 June 2011.
24. Bosma, B.; Zhang, Z.; Brekken, T.K.A.; Özkan-Haller, H.T.; McNatt, C.; Yim, S.C. Wave energy converter modeling in the frequency domain: A design guide. In Proceedings of the 2012 IEEE Energy Conversion Congress and Exposition (ECCE), Raleigh, NC, USA, 15–20 September 2012; pp. 2099–2106.
25. Bosma, B.; Brekken, T.K.A.; Özkan-Haller, H.T.; Yim, S.C. Wave energy converter modeling in the time domain: A design guide. In Proceedings of the 1st IEEE Conference on Technologies for Sustainability, Portland, OR, USA, 1–2 August 2013; pp. 103–108.
26. Law, Y.Z.; Santo, H.; Lim, K.Y.; Chan, E.S. Deterministic wave prediction for unidirectional sea-states in real-time using Artificial Neural Network. *Ocean Eng.* **2020**, *195*, 106722. [[CrossRef](#)]
27. Desouky, M.A.A.; Abdelkhalik, O. Wave prediction using wave rider position measurements and NARX network in wave energy conversion. *Appl. Ocean Res.* **2018**, *82*, 10–21. [[CrossRef](#)]
28. Kumar, N.K.; Savitha, R.; Al Mamun, A. Regional ocean wave height prediction using sequential learning neural networks. *Ocean Eng.* **2017**, *129*, 605–612. [[CrossRef](#)]
29. Zheng, C.; Li, C. Variation of the wave energy and significant wave height in the China Sea and adjacent waters. *Renew. Sustain. Energy Rev.* **2015**, *43*, 381–387. [[CrossRef](#)]
30. Avila, D.; Marichal, G.N.; Padron, I.; Quiza, R.; Hernandez, A. Forecasting of wave energy in Canary Islands based on Artificial Intelligence. *Appl. Ocean Res.* **2020**, *101*, 102189. [[CrossRef](#)]
31. Wang, Y. Efficient prediction of wave energy converters power output considering bottom effects. *Ocean Eng.* **2019**, *181*, 89–97. [[CrossRef](#)]
32. Halliday, J.R.; Dorrell, D.G.; Wood, A.R. An application of the Fast Fourier Transform to the short-term prediction of sea wave behaviour. *Renew. Energy* **2011**, *36*, 1685–1692. [[CrossRef](#)]
33. Davis, A.F.; Fabien, B.C. Wave excitation force estimation of wave energy floats using extended Kalman filters. *Ocean Eng.* **2020**, *198*, 106970. [[CrossRef](#)]
34. Ni, C.; Ma, X.; Wang, J. Integrated deep learning model for predicting electrical power generation from wave energy converter. In Proceedings of the 25th International Conference on Automation and Computing (ICAC), Lancaster University, Lancaster, UK, 5–7 September 2019; pp. 192–197.
35. Peng, J. Study on Hydrodynamic Performance for Oscillating Float Buoy Wave Energy Converter. Doctor's Dissertation, Shandong University, Jinan, China, May 2014.
36. Falnes, J. A review of wave-energy extraction. *Mar. Struct.* **2007**, *20*, 185–201. [[CrossRef](#)]
37. Hornik, K. Approximation capabilities of multilayer feedforward networks. *Neural Netw.* **1991**, *4*, 251–257. [[CrossRef](#)]
38. Ma, X.; Guan, Y.; Mao, R.; Zheng, S.; Wei, Q. Modeling of lead removal by living *Scenedesmus obliquus* using backpropagation (BP) neural network algorithm. *Environ. Technol. Innov.* **2021**, *22*, 101410. [[CrossRef](#)]